RSC Advances

PAPER

View Article Online
View Journal | View Issue

Cite this: *RSC Adv.*, 2026, **16**, 24128

Synthesis, structure, and antimicrobial activity of a series of novel heterocyclic azo-colorants derived from α-dicarbonyl compounds

Thi Ngoc Anh Vu,[ab] Nadezhda Polyanskaya,[cde] Svetlana Bozhenkova,[di] Viktor Khrustalev,[cf] Andrey Utenyshev,[dg] Anton Shetnev,[h] Igor Filenko,[i] Minh Chin Huynh,[j] Anh Van Nguyen *[k] and Olga Kovalchukova[cd]

Six novel azo-compounds derived from α-dicarbonyl species, such as 9,10-phenanthrene quinone, squaric acid and ammonium 2,3,5,6-tetraoxo-4-nitropyridinate, were isolated by reactions with a series of heterocyclic hydrazides and characterized by a set of methods. The spectral studies (FT-IR and ^{1}H NMR), together with theoretical DFT modeling and X-ray structure description, of two compounds revealed the hydrazone tautomeric forms of the molecules. Antimicrobial activity against biofilm-forming bacteria was assessed using a turbidimetric method. Growth inhibition was monitored to determine the minimum inhibitory concentration (MIC) and minimum bactericidal concentration (MBC) for both Gram-positive and Gram-negative strains. The possibility of a hemolytic effect of the compounds on human red blood cells was evaluated. The ADMET analysis indicated that all the studied compounds obeyed Lipinski's and Veber's rules of the drug discovery pipeline and offered oral bioavailability and positive blood–brain barrier permeability, indicating their potential as therapeutic lead-like compounds. According to the Toxtree analysis, all investigated compounds were categorized as Class I, indicating they belong to the low-toxicity group. The molecular interactions and inhibitory potential underlying the antimicrobial activities of the selected compounds were investigated using molecular docking methods.

Received 26th December 2025
Accepted 19th March 2026

DOI: 10.1039/d5ra10033j

rsc.li/rsc-advances

Introduction

Bacterial infections are a growing problem worldwide, causing morbidity and mortality, mainly in developing countries. In addition, another major challenge is the increase in the number of microorganisms that develop multiple drug resistance due to antibiotic abuse.[1] Currently, major infections are caused by *Escherichia coli*, multidrug-resistant *Bacillus tuberculosis*,[2] and methicillin-resistant *Staphylococcus aureus*.[3] Bacterial resistance is an inevitable consequence of evolution, and without the constant updation of modern antibacterial agents, mankind risks returning to the pre-antibiotic era.[4] Therefore, there is a need to develop new and more effective drugs. Recently, in the synthesis of modern drugs, increasing attention has been paid to the development of heterocyclic scaffolds.[5]

Currently, there is considerable interest in the synthesis of the heterocyclic derivatives of azo dyes as potential biologically active substances in the pharmaceutical sector.[6] Heterocyclic azo compounds have been widely used as antiviral, antifungal, and antioxidant agents.[7] In addition to their medicinal properties, azo compounds are used in cell staining to visualize cellular components and metabolic processes.[8] There are numerous examples of the use of 9,10-phenanthrene quinone as a substrate for the synthesis of azo compounds.[9–18] Nevertheless, new research in this area continues to be published each year, which indicates its relevance. Ongoing research into the structure–activity relationship (SAR) and biological mechanisms of azo compounds is essential for fully realizing their therapeutic potential in healthcare.[19] Previously, we reported

[a]*Laboratory of Advanced Materials Chemistry, Institute for Advanced Study in Technology, Ton Duc Thang University, No. 19 Nguyen Huu Tho Street, Tan Phong Ward, District 7, Ho Chi Minh City, 700000, Vietnam*

[b]*Faculty of Applied Sciences, Ton Duc Thang University, No. 19 Nguyen Huu Tho Street, Tan Phong Ward, District 7, Ho Chi Minh City, 700000, Vietnam*

[c]*Peoples' Friendship University of Russia (RUDN University), 6, Miklukho-Maklaya Str., Moscow 117197, Russia*

[d]*A.N. Kosygin Russian State University, 1-3, Malaya Kaluzhskaya Str., Moscow 117997, Russia*

[e]*Petrovsky Medical University, 3, Tsuriupy Str., Moscow 117418, Russia*

[f]*Zelinsky Institute of Organic Chemistry of RAS, 47 Leninsky Prospect, 119991 Moscow, Russian Federation*

[g]*Federal Research Center of Problem of Chemical Physics and Medicinal Chemistry RAS, 1, Academician Semenov Avenue, Chernogolovka, Moscow Region, 142432, Russia*

[h]*Yaroslavl State Pedagogical University Named After K.D. Ushinsky, 108, Respublikanskaya Str., Yaroslavl, 150000, Russia*

[i]*Russian Institute for Scientific and Technical Information (VINITI RAS), 20, Usievich Str., Moscow, 125315, Russia*

[j]*Ho Chi Minh City Department of Health, Ho Chi Minh City, 700000, Vietnam*

[k]*Faculty of Food Science and Technology, Ho Chi Minh City University of Industry and Trade, Ho Chi Minh City, 700000, Vietnam. E-mail: anhnv@huit.edu.vn*

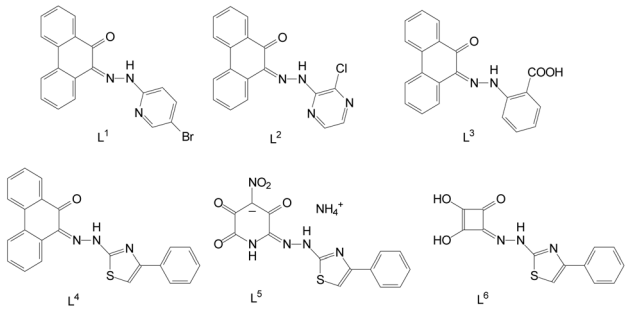

Fig. 1 Azo compounds described in the present research.

the synthesis and spectroscopic and structural properties of some azo-compounds derived from 9,10-phenanthrene quinone and their metal complexes.[20–25] The present study is devoted to the synthesis, structural and spectral investigations and antimicrobial activity of some novel azo-compounds derived from carbo- and heterocyclic α-dicarbonylic compounds (Fig. 1).

All the introduced side-chain substituents presented in the paper exhibit different types of biological activities (antibacterial, antifungal, antiviral, and antitumor for pyridine; neuroleptic, antibiotic, cardiovascular, and immunosuppressive for pyrazine; and antimicrobial, antiviral, anti-inflammatory, anesthetic, and anticonvulsant for thiazole). Of particular importance are the powerful antitumor properties of the compounds containing thiazole rings, which are being studied against various types of cancer.[26] The electron-donating properties of the N-heterocyclic atoms of the above substituents and the O-atoms of the carboxylic group in $\mathbf{L^3}$ should increase the complexing abilities of the studied compounds, which would contribute to the transport of the potential drugs in the organisms. The preservation of the biological activity of heterocyclic fragments during their transition to azo compounds was also of interest.

The reactions of the condensation of 9,10-phenanthrene quinone with different hydrazides were previously studied.[20–25] Despite the synthesis of 2,3,5,6-tetraoxo-4-nitropyridinate anion being reported more than 25 years ago,[27–29] no information on the transformation of this anion was found.

There is only little information for the corresponding reactions of squaric acid.[30] The reported compounds, $\mathbf{L^4}$–$\mathbf{L^6}$, differ only by their dicarbonyl fragments, and we expected to discover the difference in the behavior of the dicarbonyl species at condensation.

Results and discussion

Synthesis and characterization

The reported azo compounds were synthesized by the condensation of some α-dicarbonylic compounds with a series of heterocyclic hydrazides. Three α-dicarbonyl precursors were utilized in this study: commercially available 9,10-phenanthrene quinone and 3,4-dihydroxycyclobut-3-ene-1,2-dione (squaric acid), along with ammonium 2,3,5,6-tetraoxo-4-nitropyridine, synthesized according to our reported procedure.[26,27] The crystallographic and molecular characteristics, as well as the physicochemical properties of the resulting complexes, were analogous to those of 1,4-benzoquinone and its derivatives—collectively classified as six-membered pseudo-oxocarbons—as documented in the literature.[28,29]

As we noted, the coupling of hydrazides with ammonium 2,3,5,6-tetraoxo-4-nitropyridinate significantly decreased the yield of the final product compared with 9,10-phenanthrene quinone and squaric acid (from 71–93% to 35%). This may be due to a high solubility of the final product because of the ionic character of ammonium 2,3,5,6-tetraoxo-4-nitropyridinate species. The small yield of the final product in the case of $\mathbf{L^5}$ can also be explained by the structural and electronic features of 2,3,5,6-tetraoxo-4-nitropyridinate anion,[26,28] where very slight conjugation occurs between the (O)C–C(NO_2)–C(O) and (O)C–NH–C(O) fragments of the compound.

All the isolated compounds were confirmed to be chromatographically pure, with no impurities from the initial components. The primary characteristics of the azo compounds are detailed in the Experimental section.

The reliability of the molecular formulas of the synthesized compounds was determined using mass spectroscopy. The mass spectra of all compounds contained an intense molecular ion peak (m/z), which corresponded to the proposed composition, $\mathbf{L^1}$–$\mathbf{L^6}$.

The structure of the compounds could also be illustrated by ^{1}H NMR, FTIR and UV absorption spectra (Fig. S1–S12). In the FTIR spectra of the synthesized compounds, a characteristic absorbance at 1675–1654 cm^{-1} (νCO) indicated the hydrazo-form of all the studied compounds in the solid state. The C═O absorption bands were strongly shifted to low frequencies. This agreed with the involvement of carbonyl groups in strong intramolecular H-bonds.

The ^{1}H NMR spectra of the DMSO solutions of compounds $\mathbf{L^1}$–$\mathbf{L^6}$ revealed characteristic proton signals across several regions. The 3.3 ppm (singlet) signal in the spectrum of $\mathbf{L^3}$ was related to a proton of the carboxylic group.[31] The multiplets in the 8.50–7.25 ppm range for all the compounds indicated benzene rings in all studied molecules. Singlet signals at 16.20–15.57 ppm were assigned to the NH protons of the hydrazo group. The signal at 3.7 ppm in the ^{1}H NMR spectrum of $\mathbf{L^5}$ may be assigned to the protons of the NH_4^+ cation.

Tautomerism of azo-compounds derived from α-dicarbonyl compounds

Theoretically, the studied molecules could exist in the form of three tautomers: azo (c), hydrazo (b), and zwitter-ionic (a), where the "mobile" hydrogen atom was localized at an N-atom of a heterocyclic fragment of the molecules. Each of the tautomers was characterized by four more structures due to *cis–trans* isomerism involving exocyclic N–C bonds (Fig. S20). It should be noted that no zwitterionic tautomers are available for $\mathbf{L^3}$. DFT calculations performed for $\mathbf{L^1}$–$\mathbf{L^6}$ as an example indicated the highest stability of the b(s-*cis*, *cis*) tautomers. The *trans*-isomers turned into corresponding *cis*-isomers at optimization. The relative energies of the corresponding isomers of $\mathbf{L^1}$–$\mathbf{L^6}$ are presented in Table S1.

As it is evident from Table S1, for all the compounds, except L^2 and L^5, the hydrazo-forms are the most stable tautomers. For L^2, the energies of *cis*- and *trans*-forms were equal, and for L^5, the azo-tautomer was only 9.04 kJ per mole less than the corresponding hydrazo-form. This may indicate easy hydrazo–azo tautomerism in L^2 and L^5 and explain the absence of the signal of a proton of the NH hydrazo group in the ^{1}H NMR spectrum of L^5.

The optimized structures of the most stable hydrazo-tautomers and some calculated bond lengths for L^{1-6} are presented in Fig. 2.

As it is evident from Fig. 2, the hydrazo-forms of L^2, L^2, L^4, and L^5 are stabilized by intermolecular NH···O=C hydrogen bonds with H···O distances of 1.793, 1.765, 1.755 and 1.500 Å for L^2, L^2, L^4, and L^5, respectively. The shortest distance in the case of L^5 may indicate a transitional state between the hydrazo- and azo-forms of the molecule, which suggests similar stabilities of these tautomers. For L^3, the proton of the hydrazo-group was stabilized by two intermolecular H-bonds: C=O···HN (1.858 Å) and HO–C=O···HN (1.973 Å). In the optimized structure of L^6, no intermolecular H-bonds were calculated.

The close values of energies of the *cis*- and *trans*-isomers may lead to *cis–trans* isomerization in solutions. In polar solvents and at alkaline pH values, the azo-forms were more preferable, and long-wave adsorption bands in UV-vis spectra shifted bathochromically. This was shown using L^5 as an example (Fig. S12).

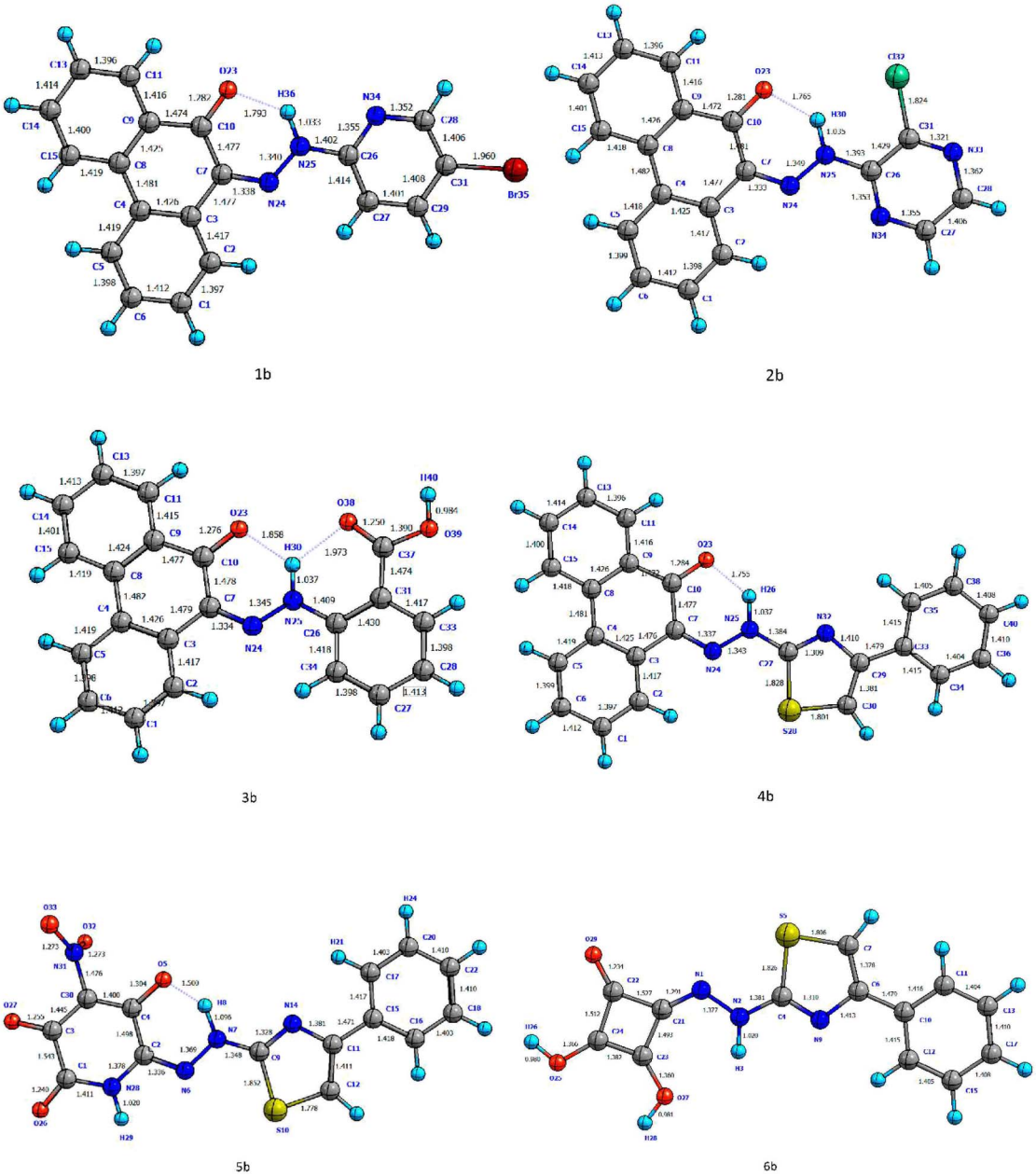

Fig. 2 DFT-optimized structure and some bond lengths of L^{1-6} (dashed lines indicate H-bonds).

Crystal and molecular structures of L^2 and L^4

The hydrazo-tautomeric forms of the azo-compounds derived from 9,10-phenanthrene quinone were proved by X-ray analysis on single crystals of L^2 and L^4 (Fig. 3). The H atom in both structures was localized at the N1 atom of the azo fragments of the molecules.

The molecules were stabilized by intramolecular N1H···O1 bonds: N1–H 1.06(8) and 0.77(7), O1···H 1.73(9) and 1.97(7), N1···O1 2.551(8) and 2.556(6) Å; ∠ O1HN1 131(7) and 133(7) deg. for L^2 and L^4, respectively. Rather short Cl1H (2.49 Å) and N3H (2.51 Å) contacts were additionally found for L^2 and L^4, respectively.

The bond lengths in the molecules were standard and did not deviate from those reported (CO 1.240(8) and 1.253(6); N1N2 1.326(8) and 1.338(6); N1C2(C1) 1.395(9) and 1.379(7); N2C12(C5) 1.332(9) and 1.313(7) Å for L^2 and L^4, respectively) [9, 10, 20, 22]. It should be noted that there was a significant delocalization in the C2(C1)N1N2C12(C5) fragments of the studied molecules. This led to almost planar structures of both molecules, with the screw angles between phenanthroline and heteroatomic cycles being 4.5(3) and 4.4(3) deg. for L^2 and L^4, respectively. The benzene ring was turned around the planar part of L^4 by 14.1(3) deg.

The phthalazine fragments in L^2 and L^4 were oriented relative to the N1–N2 azo group in a way where the C1–N3 bond in L^2 was in the *cis*-position, and the C2–N3 bond in L^4 was in the *trans*-position (the torsion N3C1N1N2 and N3C2N1N2 angles were −1.3(11) and −179.1(5) deg. for L^2 and L^4, respectively).

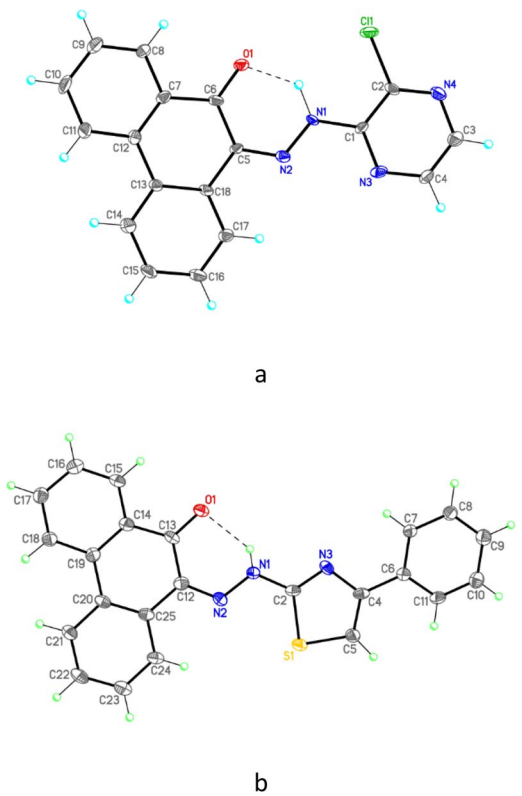

Fig. 3 Molecular structures of L^2 (a) and L^4 (b) (50% ellipsoids). The dashed line indicates the intramolecular N–H···O hydrogen bond.

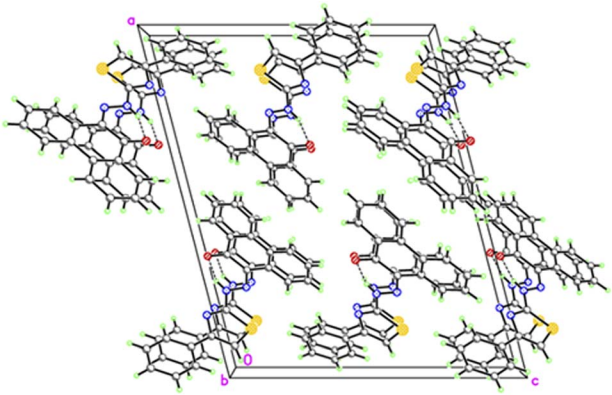

Fig. 4 Crystal structure of L^2 along the crystallographic *c* axis. Dashed lines are indicative of the intra- and inter-molecular hydrogen bonds.

In the crystal of L^2, the molecules were bound to each other by the weak intermolecular C4–H4···N3 ($2 - x$, $1 - y$, $z + 1/2$) [C···N 3.366(9) Å, H···N 2.50 Å, ∠C–H···N 152°] hydrogen bonding interactions, converting into spiral double-stacks along the crystallographic *c* axis. The double-stacks were arranged at van-der-Waals distances; thus, they could not avoid the π,π-stacking between the planar parallel fragments in the columns (Fig. 4).

In the crystal of L^4, the molecules formed stacks along the crystallographic *b* axis. The stacks were arranged at van-der-Waals distances; thus, they could not avoid the π,π-stacking between the planar parallel fragments in the columns (Fig. 5).

The mean distances between the aromatic fragments of the neighboring molecules in the columns were 3.34–3.35 Å for L^2 and 3.62–3.67 Å for L^4. This may indicate the existence of π,π-stacking between the planar parallel fragments in the columns, which stabilized the lattice structure. The neighboring columns were almost perpendicular to each other in L^4 and formed an angle of 120 deg. in L^2.

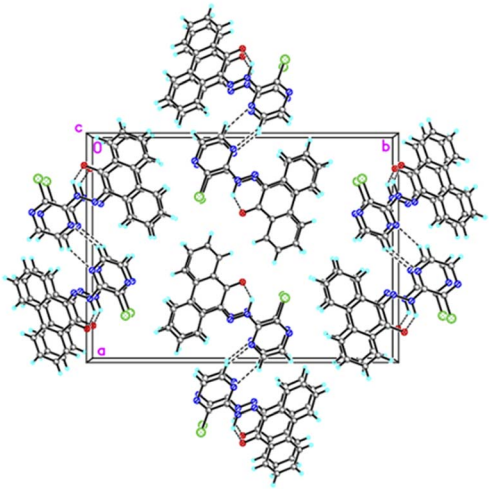

Fig. 5 Crystal structure of L^4 along the crystallographic *b* axis. The dashed lines are indicative of the intramolecular hydrogen bonds.

Antimicrobial activity

The L^{1-6} compounds were tested in triplicate against a panel of microorganisms. Gram-negative strains included *Escherichia coli* C1 (Fig. S13 and S14), *E. coli* F, and *Pseudomonas fluorescens* A1. Gram-positive strains included *Staphylococcus aureus* ATCC-25923 (Fig. S15 and S16), a clinical isolate of *S. aureus*, *Bacillus cereus* IP 5832, *Enterococcus faecium* K-1, and *Micrococcus luteus* 2665. The compounds were also tested against the fungus *Candida albicans* ATCC 10231. The compounds were studied as suspensions in the concentration range of 256–0.25 μg mL^{-1} (0.5% DMSO). Two active compounds, namely L^3 and L^4, were revealed.

For the L^3 and L^4 compounds, the ratio of the minimum bactericidal concentration to the minimum inhibitory concentration was 4 or more, which allowed us to conclude that the substances were bacteriostatic. The MIC and MBC values of the studied compounds are presented in Table 1.

To study the possible toxic effects of L^3 and L^4, a series of experiments were carried out. The hemolytic activity, which consisted of the ability to destroy the membrane of erythrocytes 0(1) of the human blood (RBC) was studied. It was shown that L^3 and L^4 did not have a significant hemolytic effect on human red blood cells (Table S2) and retained their antimicrobial properties when stored as solutions for more than a week.

The anti-biofilm activities of L^3 and L^4 in relation to the preformed clinical isolates of Gram-positive (*S. aureus*, *Enterococcus faecium* K-1) and Gram-negative (*Pseudomonas fluorescens* A1) bacteria were not detected. The compounds studied presumably did not have the ability to actively interact with the exopolysaccharide intercellular matrix of the formed bacterial biofilms, which was apparently determined by the absence of highly reactive functional groups on the surface. However, the L^3 sub-inhibitory concentrations of 0.25 μg mL^{-1} and 0.12 μg mL^{-1} prevented the formation of bacterial biofilms *in vitro* against Gram-positive bacteria, *Staphylococcus aureus*, clinically by 67% and 50%, respectively, and against Gram-negative bacteria, *Pseudomonas fluorescens* A1, by 34% and 58%, respectively.

Thus, the obtained data indicated the high antimicrobial activity of L^3 and L^4 against Gram-positive and Gram-negative bacteria, good stability, and safety.

Molecular docking simulation

As determined by the antimicrobial test, ligands L^3 and L^4 presented excellent antibacterial activity. Therefore, the antibacterial activities of both molecules were simulated through docking studies to provide a better understanding of the molecular interaction. To mechanistically characterize the observed broad-spectrum antibacterial activity, a panel of six essential or virulence-associated protein targets was selected from the tested microbial species. This diverse set of targets was chosen to model the multiple potential modes of action across both Gram-positive and Gram-negative bacteria, focusing on critical pathways for survival and defense. The selected Protein Data Bank (PDB) structures and their corresponding mechanisms were as follows. For genome integrity, the DNA Gyrase B N-terminal fragment (4PRV) from *Escherichia coli* was selected as the prototypical target for interfering with bacterial DNA topology, a classical mechanism of action for broad-spectrum agents. For cell envelope and membrane synthesis, two highly essential pathways were represented: the fatty acid synthesis (FAS-II) enzyme, FabI (1JIL), from *Staphylococcus aureus* and the SCWP *O*-acetyltransferase PatB1 (5V8E) from *Bacillus cereus*, the latter being crucial for S-layer protein attachment and cell wall integrity. Additionally, the D-alanylating protein ligase DltA (1GWE) from *Micrococcus luteus* was included to model interference with cell surface charge and teichoic acid modification. To assess the interaction with bacterial defense and metabolic pathways, two specific targets were included: the pediocin-like immunity protein EntA-im (2BL8) from *Enterococcus faecium*, presenting the potential disruption of resistance or cell surface protection mechanisms; and the HutD bicupin protein (5V00) from *Pseudomonas fluorescens*, which was involved in histidine metabolism and cellular regulation, suggesting a potential role in nutrient scavenging inhibition. Utilizing protein IDs specific to the tested organisms ensured that the predicted binding poses and affinities were structurally relevant to the observed biological activity. The results of the binding affinities and interacting residues of two ligands, $L^{3,4}$, with these proteins are shown in Table 2 and Fig. S17.

Molecular docking simulations were performed to elucidate the mechanistic basis for the observed broad-spectrum

Table 1 MIC and MBC values for L^{1-6}

		MIC[a], μg mL^{-1}				MBC[a], μg mL^{-1}			
Type	Microbials	$L^{1,2,5,6}$	L^3	L^4	Pef[b]	$L^{1,2,5,6}$	L^3	L^4	Pef[b]
Gram-positive	*Staphylococcus aureus*	—	8	8	2	—	—	—	2
	Staphylococcus aureus ATCC-25923	—	0.5	8	2	—	4	32	2
	Bacillus cereus IP 5832	—	1	16	2	—	128	256	2
	Enterococcus faecium K-1	—	0.5	32	2	—	4	256	2
	Micrococcus luteus 2665	—	1	32	2	—	4	256	2
Gram-negative	*Escherichia coli* C1	—	256	256	2	—	—	—	2
	Escherichia coli F	—	0.5	32	2	—	4	64	2
	Pseudomonas fluorescens A1	—	1	2	2	—	4	8	2
Fungi	*Candida albicans* ATCC 10231	>256	32	32	2	—	—	—	2

[a] The minimum inhibitory and bactericidal concentrations (MIC and MBC) of the test compounds were determined using the broth microdilution method over a concentration range of 0.5–256 μg mL^{-1}. [b] Pefloxacin (Pef) was used as the positive control antibiotic.

Table 2 Binding affinities and interacting residues of L^3 and L^4 against various proteins

Protein ID	Binding affinity (kcal mol^{-1})	Hydrogen bond	Hydrophobic
L^3			
5V8E (*B. cereus*)	−9.177	Leu210	Tyr187 and Ala233
2BL8 (*E. faecium*)	−9.138	Lys37, Arg94, His10, and Tyr35	Leu50, Tyr43, Lys6, and Pro49
4PRV (*E. coli*)	−9.703	Tyr109 and Arg76	Ala47, Ile78, Ile94, Asn46, and Pro79
1JIL (*S. aureus*)	−9.517	Gly38 and Gln174	Leu70 and His50
1GWE (*M. luteus*)	−12.535	Arg339 and Asn133	Ala118, Tyr343, Ala346, Arg58, Val131, Ala342, and Pro60
5V00 (*P. fluorescens*)	−10.215	Thr24 and Arg41	Trp17, Phe53, and Ala45
L^4			
5V8E (*B. cereus*)	−8.718	—	Leu210, Ala233, and Leu210
2BL8 (*E. faecium*)	−9.18	Arg94 and Lys37	Pro49 and Tyr43
4PRV (*E. coli*)	−8.278	Gly102	Pro79 and Ile94
1JIL (*S. aureus*)	−9.298	Asp195	Leu233, Val224, Pro53, and Leu52
1GWE (*M. luteus*)	−12.839	—	Phe138, Phe146, Gly338, Tyr343, Ala118, and Arg58
5V00 (*P. fluorescens*)	−10.019	Arg41	Trp17, Phe53, and Ala45

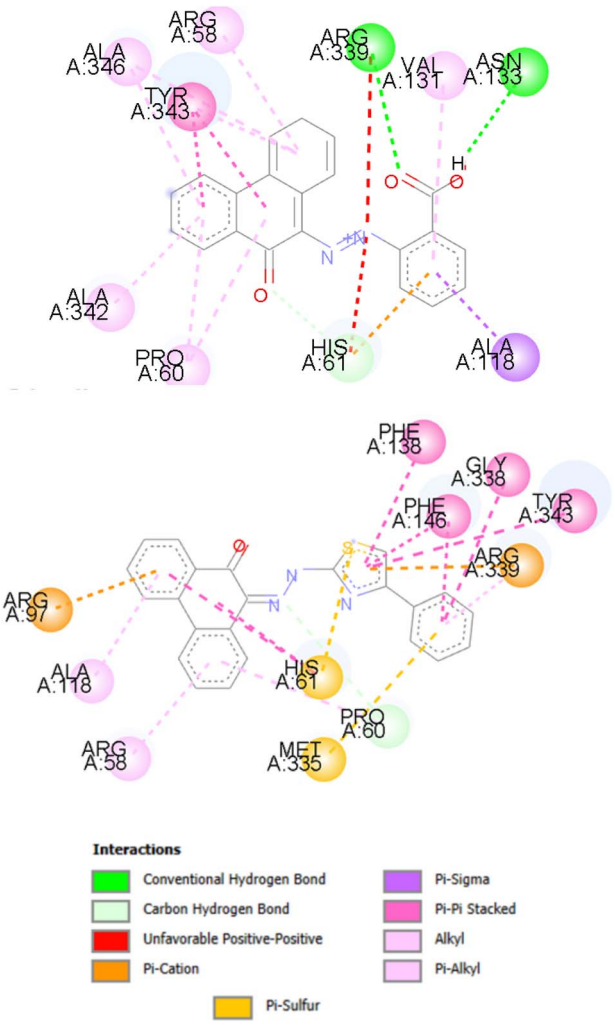

Fig. 6 2D chemical structures representing the protein-ligand (1GWE) interactions of L^3 and L^4.

antibacterial activities of compounds L^3 and L^4. The binding affinity values against the six protein targets ranged from −6.278 to −12.839 kcal mol^{-1}, with compound L^3 generally demonstrating relatively high affinity values against most targets, particularly against DltA (1GWE) (−12.535 kcal mol^{-1}). Although L^4 showed a slightly stronger interaction with 1GWE (−12.839 kcal mol^{-1}), the overall binding profile suggested that L^3 established more energetically favorable interactions across the protein panel, correlating with its superior MIC values observed experimentally. The superposition of L^3 and L^4 within the active site of 1GWE (Fig. 6) clearly illustrated the shift from the hydrogen-bond-dominated stabilization of the hydrazone scaffold to the Pi-interaction-driven binding of the thiazole derivative.

The binding modes revealed significant differences in the stabilization mechanisms driven by the distinct scaffold structures (hydrazone for L^3 and thiazole for L^4). Compound L^3 primarily utilized a network of conventional hydrogen bonds with polar residues, such as GLY A:38 and GLN A:174 in FabI (1JIL) and THR A:24 and ARG A:41 in HutD (5V00). This hydrogen bonding capacity allowed L^3 to anchor effectively within the active sites, overcoming some unfavorable acceptor interactions observed in FabI and unfavorable positive–positive repulsion in the immunity protein (2BL8). In contrast, L^4 heavily relied on extended Pi-cation interactions with positively charged residues, LYS and ARG. Key examples include the strong Pi-cation bond with LYS A:103 in GyrB (4PRV) and multiple Pi-cation bonds with ARG/HIS in DltA (1GWE). Although the Pi-cation interactions in L^4 are generally strong and favored, the more robust and traditional hydrogen bonding profile of L^3 likely provides a more rigid and specific orientation within the binding sites of crucial metabolic enzymes, which may better explain its overall enhanced potency against the microbial panel. Furthermore, both compounds demonstrated effective Pi–Pi and Pi-alkyl stacking, particularly with TRP in HutD and TYR in DltA, suggesting that hydrophobic forces

played a critical role in stabilizing the complexes across all tested species.

The binding affinity of the two synthesized compounds when attached to six selected proteins ranged from 8.718 to 12.839 kcal mol^{-1}, with compound L^3 generally exhibiting the highest affinity. Compound L^3 demonstrated a very strong binding affinity, with most interactions being conventional hydrogen bonding. The molecular docking simulations successfully elucidated the potential binding modes of L^3 and L^4; however, these findings represented computational predictions. Subsequent work will focus on experimental validation through enzyme inhibition assays and binding affinity measurements to confirm the proposed pharmacodynamic adjustments.

ADMET scan

The physicochemical property; medicinal chemistry; and the absorption, distribution, metabolism, excretion, and toxicity (ADMET) computations are considered as an initial phase in the pipeline of drug design/discovery.[32–34] Fig. 7 provides information on important ADME-related properties of synthetic ligands and Lipinski's rule of five (molecular weight ≤ 500; MLOGP ≤ 4.15; number of (N + O) ≤ 10; number of (NH + OH) ≤ 5 (ref. 33)). None of the compounds showed any violations against the Lipinski (Pfizer) filter for drug delivery.

Some pharmacokinetic properties of L^1–L^6 are presented in Table 3. As displayed in Table 3, all the compounds, except L^5, were predicted to have high gastrointestinal (GI) absorption (human intestinal absorption; HIA). The low activity of L^5 in GI absorption may be explained by the ionic character of the molecule. Among the studied compounds, only L^1 could cross the blood–brain barrier (BBB), and none of them was a substrate of P-glycoprotein (P-gp).

Cytochrome P450 (CYP450) enzymes mediate phase I of xenobiotic metabolism and determine the pharmacokinetic fate of drugs in our body. All the studied compounds were computationally checked for the categorization of inhibitors or the substrates of CYP450 enzymes to predict their adverse drug events and drug–drug interactions (Table 4).[35,36] Based on the results of Toxtree, all the compounds belonged to class low (Class IV) toxic compounds (Table 4).

The hemolysis assay was used as a first-pass indicator of the potential membrane-disruptive effects of the synthesized compounds. It should be noted that erythrocyte lysis does not substitute cytotoxicity profiling in nucleated mammalian cells, which will be required for a comprehensive safety assessment. Nonetheless, considered alongside MIC/MBC data, the hemolysis readout provided a practical, qualitative estimate of the selectivity window of the lead structures.

The predicted acute oral toxicities for compounds L^1–L^6 of 526.6–2354.0 mg kg^{-1}. These results place the compounds in toxicity Class 4, comparable to the clinically used antimicrobial pefloxacin. While classified as low toxicity, pefloxacin is known to potentially cause gastrointestinal, neurological, and musculoskeletal issues, as well as serious eye irritation.

Experimental

Materials

All reagents were sourced from Sigma Chemical Co., USA, and used without any further purification. The chemical details are as follows: 9,10-phenanthrene quinone (95% purity; CAS: 84-11-7, $C_{14}H_8O_2$, 208.21 g mol^{-1}), 5-bromo-2-hydrazinopyridine (97% purity; CAS: 77992-44-0, $C_5H_6BrN_3$, 188.03 g mol^{-1}), 2-chloro-3-hydrazinopyrazine (95% purity; CAS: 63286-28-2, $C_4H_5ClN_4$, 144.56 g mol^{-1}), 2-hydrazine benzoic acid hydrochloride (96%

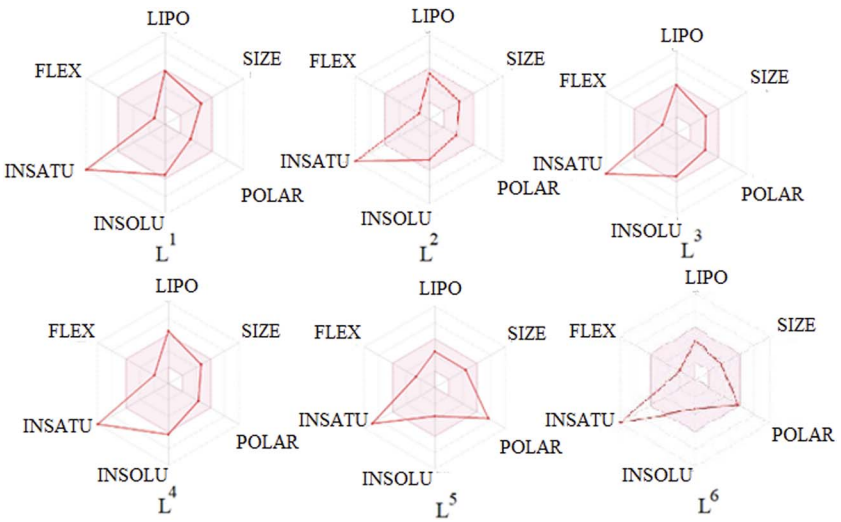

Fig. 7 Bioavailability radars illustrating the drug-likeness profiles of compounds L^1–L^6 based on key physicochemical properties. The pink area represents the optimal range for physicochemical properties lipophilicity: XLOGP3 between −0.7 and +5.0, size: MW (molecular weight) between 150 and 500 g mol^{-1}, polarity: TPSA (topological polar surface area) between 20 and 130 $Å^2$, solubility: log *S* not higher than 6, saturation: fraction of carbons in the Csp^3 hybridization not less than 0.25, and flexibility: no more than 9 rotatable bonds.

Table 3 Some pharmacokinetic properties of L^1–L^6[a]

Comp.	GI absorption	BBB permeant	P-gp substrate	Cytochrome P450 inhibition				
				CYP1A2	CYP2C19	CYP2C9	CYP2D6	CYP3A4
L^1	High	Yes	No	Yes	Yes	Yes	No	No
L^2	High	No	Yes	Yes	Yes	Yes	Yes	Yes
L^3	High	No	No	Yes	No	Yes	No	No
L^4	High	No	No	Yes	Yes	Yes	No	No
L^5	Low	No	No	No	No	No	No	No
L^6	High	No	No	Yes	No	No	No	No

[a] GI: gastrointestinal; BBB: blood–brain barrier; P-gp: P-glycoprotein; CYP: cytochrome.

Table 4 Prediction of the acute toxicity of L^1–L^6

Compound	Acute toxicity with intravenous administration (mg kg^{-1})	Toxicity class	Acute toxicity following oral administration (mg kg^{-1})	Toxicity class
L^1	161 100	4	1 761 000	4
L^2	1 069 000	5	526 600	4
L^3	235 200	4	1 908 000	4
L^4	144 400	4	2 354 000	5
L^5	162 200	4	879 000	4
L^6	453 900	4	853 400	4

purity; CAS: 52356-01-1, $C_7H_9ClN_2O_2$, 188.61 g mol^{-1}), 2-hydrazino-4-phenylthiazole (97% purity; CAS: 34176-52-8, $C_9H_9N_3S$, 191.25 g mol^{-1}), 2,3,5,6-tetraoxo-4-nitropyridinate, isolated according to the procedure described[26] (95% purity), and 3,4-dihydroxy-3-cyclobutene-1,2-dione (99% purity; CAS: 2892-51-5, $C_4H_2O_4$, 114.06 g mol^{-1}).

Synthesis

10-(2-(5-Bromopyridine-2-yl)hydrazinylidene)phenanthrene-9(10*H*)-one (L^1). A solution of 0.5 g (2.4 mmol) of 9,10-phenanthrene quinone in 40 mL of DMF was supplemented with 5 mL of 96% sulfuric acid. The reaction mixture was cooled to room temperature, and 0.45 g (2.4 mmol) of 5-bromo-2-hydrazinopyridine was added in portions with constant stirring. After 2 hours, the orange precipitate was filtered off, rinsed with water, and dried in air. 0.66 g (1.7 mmol) of L^1 compound was obtained (yield: 71%) in the form of bright orange crystals. R_f 0.81; M.P. 201–202 °C; $C_{19}H_{12}BrN_3O$; calculated/found, %: C: 60.34/59.66; H: 3.20/3.19; N: 11.11/10.91; Br: 21.12/21.05; ^{1}H NMR, ppm: 15.57 (s); 8.42–7.28 (m); FT-IR, cm^{-1}: 1668; 1597; 1575; 1498; 1469; 1447; UV-vis, nm/ε: 465/2.25 × 10^4. *m*/*z*: 380.

10-(3-(2-Chloropyrazine-2-yl)hydrazinylidene)phenanthrene-9(10*H*)-one (L^2). 10 mL of 96% sulfuric acid was added dropwise to a solution of 1.04 g (5.0 mmol) of 9.10-phenanthrene quinone in 80 mL of DMF. The reaction mixture was cooled to room temperature, and a solution of 0.72 g (5.0 mmol) of 2-chloro-3-hydrazinopyrazine in ethanol was added in batches with constant stirring. After 4 hours, the reaction mixture was poured into an aqueous solution of sodium carbonate until a slightly alkaline medium of the final mixture was created. The orange precipitate was filtered off, washed with water, dried, and purified by recrystallization from chloroform. 1.40 g (4.2 mmol) of the L^5 compound (yield: 84%) was obtained in the form of bright orange crystals; R_f 0.32, M.P. 221–222 °C; $C_{18}H_{11}ClN_4O$, calculated/found, %: C: 64.58/64.20; H: 3.31/3.37; N: 16.74/16.90; ^{1}H NMR, ppm: 15.58 (s); 8.42–7.28 (m); FT-IR, cm^{-1}: 1674; 1626; 1599; 1560; 1492; 1446; UV-vis, nm/ε: 459/2.5 × 10^4. *m*/*z*: 334.

2-(2-(10-Oxophenanthrene-9(10*H*)-ylidene)hydrazinyl) benzoic acid (L^3). A solution of 0.52 g (2.5 mmol) of 9.10-phenanthrene quinone in 40 mL of DMF was added dropwise to 6 mL of 96% sulfuric acid. The reaction mixture was cooled to room temperature, and a solution of 0.47 g (2.5 mmol) of 2-hydrazine benzoic acid hydrochloride in ethanol was added in portions with constant stirring. After 3 hours, the reaction mixture was poured into an aqueous solution of sodium carbonate until a slightly alkaline medium of the final mixture was created. The orange precipitate was filtered off, washed with water, dried in air, and purified by recrystallization from chloroform. 0.76 g (2.2 mmol) of the L^2 compound (yield: 89%) was obtained in the form of reddish-orange crystals; R_f 0.59, M.P. 264–265 °C; $C_{21}H_{14}N_2O_3$; calculated/found, %: C: 73.67/72.98; H: 4.12/4.13; N: 8.18/7.37; ^{1}H NMR, ppm: 16.20 (s); 8.50–7.25 (m); 3.3 (s); FT-IR, cm^{-1}: 3069; 1675; 1598; 1572; 1487; 1445; 1413; UV-vis, nm/ε: 483/1.4 × 10^4. *m*/*z*: 342.

10-(2-(4-Phenyl thiazo-2-yl) hydrazinylidene) phenanthrene-9(10*H*)-one (L^4). 10 mL of 96% sulfuric acid was added dropwise to a solution of 1.04 g (5.0 mmol) of 9.10-phenanthrene quinone in 80 mL of DMF. The reaction mixture was cooled to room temperature, and a solution of 0.96 g (5.0 mmol) of 2-hydrazino-4-phenylthiazole in ethanol was added in batches with constant stirring. After 3 hours, the reaction mixture was poured into an

aqueous solution of sodium carbonate until a slightly alkaline medium of the final mixture was created. The red precipitate was filtered off, washed with water, dried, and purified by recrystallization from chloroform. 1.77 g (4.6 mmol) of the $\mathbf{L^3}$ compound (yield: 93%) was obtained in the form of dark red crystals; R_f 0.32, M.P. 221–222 °C; $C_{23}H_{15}N_3OS$ calculated/found, %: C: 72.42/71.41; H: 3.96/3.97; N: 11.01/10.92; S: 8.40/8.06; ^{1}H NMR, ppm: 15.58 (s); 8.42–7.28 (m); FT-IR, cm^{-1}: 1672; 1597; 1527; 1499; 1489; 1442; UV-vis, nm/ε: 497/2.3 × 10^4. *m*/*z*: 381.

4-Nitro-2,3,5-trioxo-6-(2-(4-phenyl thiazole)-2-yl) hydrozinilydene pyperidine-4-yde ($\mathbf{L^5}$). 4 mL of 96% sulfuric acid was added dropwise to a solution of 0.46 g (2.3 mmol) of ammonium 2,3,5,6-tetraoxo-4-nitropyridinate (isolated according to the described procedure[26]) in 40 mL of a 1 : 1 mixture of ethanol and DMF. The reaction mixture was cooled to room temperature, and 0.44 g (2.3 mmol) of 2-hydrazino-4-phenylthiazole was added in portions with constant stirring. After 3 hours, the reaction mixture was poured into an aqueous solution of sodium carbonate until a slightly alkaline medium of the final mixture was created. The dark-colored precipitate was filtered, washed with water, dried, and purified by recrystallization from chloroform. 0.29 g (0.8 mmol) of the $\mathbf{L^4}$ compound (yield: 35%) was obtained in the form of maroon crystals; R_f 0.71, M.P. 157–158 °C; $C_{14}H_{12}N_6O_5S$ calculated/found, %: C: 44.44/44.62; H: 3.73/3.47; N: 22.21/21.54; S: 8.47/8.58; ^{1}H NMR, ppm: 8.1–7.3 (m); 3.7 (s); FT-IR, cm^{-1}: 1654; 1595; 1540; 1492; 1355; UV-vis, nm/ε: 459/4.5 × 10^4, *m*/*z*: 376.

(4*Z*)-2,3-dihydroxy-4-[2-(5-phenyl-1,3-thiazol-2-yl)hydrazin-1-ylidene]cyclobut-2-en-1-one ($\mathbf{L^6}$). A solution of 0.29 g (2.5 mmol) of 3,4-dihydroxy-3-cyclobutene-1,2-dione and a solution of 0.48 g (2.5 mmol) of 2-hydrazino-4-phenylthiazole were dissolved separately in 15 mL of alcohol. After complete dissolution, the solutions were mixed, and 1 mL of sulfuric acid was added. The solutions of α-dicarboxylic compound and hydrazine were colorless, but after mixing, the solution turned purple. After an hour, the solution became more intense in color. After 2 hours, the reaction mixture was poured into an aqueous solution of sodium carbonate until a slightly alkaline medium of the final mixture was created. The red-purple precipitate was filtered off, washed with water, dried in air, and purified by recrystallization from chloroform. 0.58 g (2.0 mmol) of the $\mathbf{L^6}$ compound (yield: 80%) was obtained in the form of bright dark-purple crystals; R_f 0.85, M.P. 236–237 °C; $C_{13}H_9N_3O_3S$ calculated/found, %: C: 54.36/54.20; H: 3.14/3.37; N: 14.63/14.90; S: 11.15/10.95; ^{1}H NMR, ppm: 15.58 (s); 8.42–7.28 (m); FT-IR, cm^{-1}: 1750; 1699; 1599; 1570; 1488; 1446; UV-vis, nm/ε: 652/2.3 × 10^4, *m*/*z*: 287.

Melting point determination

A small amount of a finely ground, well-dried azo compound sample was placed in a thin-walled glass capillary (45–50 mm in length and 0.8–1.0 mm in diameter) sealed at one end. After establishing a stable temperature within the apparatus chamber, the capillaries were placed inside, the heating rate was adjusted, and the melting temperatures were recorded.

Thin-layer chromatography

The purity of the isolated compounds was controlled by thin-layer chromatography on an aluminum TLC plate coated with a layer of aluminum oxide. A mixture of benzene and ethanol (4 : 1) was used as an eluent. The development of chromatograms was carried out under UV light (255 nm).

Analysis methods

Elemental analysis for C, H, S and N was conducted using a Varian 735-OES elemental analyzer. Mass spectra were obtained with an ESI-TOF instrument. Fourier transform infrared (FTIR) spectra were recorded on a PerkinElmer FT-IR 1650 spectrometer in the 4000–400 cm^{-1} range, using KBr pellets. UV-vis spectra were measured with a Varian Cary 50 Scan spectrophotometer. ^{1}H NMR spectra (DMSO-d6 solutions) were recorded on a JEOL JNM-ECA 600 spectrometer with TMS as the internal reference. Solution pH was determined with a Corning pH-meter-430.

X-ray diffraction studies

The X-ray diffraction data for $\mathbf{L^2}$ and $\mathbf{L^4}$ single crystals were collected on a four-circle XtaLAB Rigaku Synergy-S diffractometer equipped with a HyPix-6000HE area-detector (T = 100 K, λ(CuKα)-radiation, graphite monochromator, shutterless ω-scan mode). The data were integrated and corrected for absorption using the CrysAlisPro program.[38] The structures were solved by the intrinsic phasing modification of direct methods[37] and refined by a full-matrix least squares technique on F^2, with anisotropic displacement parameters for non-hydrogen atoms. The hydrogen atoms of the NH groups were objectively localized in the difference-Fourier maps and refined freely with fixed isotropic displacement parameters [U_{iso}(H) = 1.2U_{eq}(N)]. The other hydrogen atoms were placed in calculated positions and refined within a riding model with fixed isotropic displacement parameters [U_{iso}(H) = 1.5U_{eq}(C) for the CH_3-groups and 1.2U_{eq}(C) for the other groups]. All calculations were carried out using the SHELXTL program suite.[39,40]

The crystallographic data for the investigated compounds have been deposited with the Cambridge Crystallographic Data Center, CCDC 2482127 ($\mathbf{L^2}$) and CCDC 2482128 ($\mathbf{L^4}$). The supplementary crystallographic data can be obtained free of charge from the Cambridge Crystallographic Data Centre *via* https://www.ccdc.cam.ac.uk/data_request/cif. The crystal and refinement data for the studied compounds are presented in Table S3.

Theoretical studies

The quantum chemical modeling of molecular and electronic structures of the organic molecules, their ionic forms, and complexes with metals was performed by the density functional theory (DFT) using the hybrid potential B3LYP[41] and a def2-SV(P) basis set[42] with full geometry optimization. All the calculations were performed with the Firefly 7.1.G software package.[43]

Scanning of molecular property descriptors

The canonical SMILES formats of the ligands were submitted to the SwissADME server (https://www.swissadme.ch/32-34), AdmetSar (https://lmmd.ecust.edu.cn/admetsar235),[36] and ADMETlab 2 (ref. 37) to compute all predictable physicochemical and medicinal chemistry attributes and target prediction. The Toxtree v2.5.1 software platform (https://toxtree.sourceforge.net/) was also employed to predict the class of toxicity.

Bactericidal studies

The antimicrobial activity of the compounds was studied by the method of serial dilution, using the turbidimetric method for monitoring the growth of microorganisms in accordance with the recommendations.

Equipment and supplies: a FlexA-200 Microplate Reader ALLSHENG Flatbed Photometer from Hangzhou Allsheng Instruments Co., Ltd; plastic sterile 96-well Nest tablets.

Investigated compounds: negative control: the substance, pefloxacin mesylate dihydrate, manufactured by Qingdao Dacon Trading Co., Ltd.

The studied strains: *Escherichia coli* C1, *Escherichia coli* F, *Staphylococcus aureus* ATCC-25923, *Staphylococcus aureus clinical*,*Bacillus cereus* IP 5832, *Enterococcus faecium* K-1, *Micrococcus luteus* 2665, *Pseudomonas fluorescens* A1, and *Candida albicans* ATCC 10231. The nutrient media: LB (Lennox) produced by Dia-M (Obninsk, Russia); LB agar (Lennox) produced by Dia-M (Obninsk, Russia).

The method of nutrient media preparation: 20 g of nutrient solution and 1 liter of freshly distilled water were placed in a 2 liter flask with a magnetic stirrer. The broth was dissolved upon heating and intensive stirring. The suspension was boiled for one minute until it was completely dissolved. The resulting solution was poured into clean containers of a suitable size and sterilized in an autoclave at 121 °C for 15 minutes. The finished medium had a transparent amber color. It was stored at a temperature of 2–8 °C. LB was used for the cultivation of the test culture strains in all cases. Cultivation was carried out in sterile tubes and flasks with cotton-gauze stoppers and Petri dishes with aeration at a temperature of 37 °C.

The method of microorganisms' cultivation: using a bacteriological loop, a single bacterial colony was removed from a plate with LB-agar, incubated at 37 °C for 16–20 hours, and transferred to a sterile flask containing 10 mL of LB. The resulting solution was incubated at 37 °C and intensively aerated (200 rpm) at night.

Preparation of exploratory preparations: stock solutions of the substance were prepared from 0.00512 g of powdered substance, 350 μL of distilled water, and 150 μL of dimethyl sulfoxide (DMSO). 5 μL of the test compound solution was injected into 200 μL wells of a 96-well tablet, followed by double dilution: 256–128–64–32–16–8–4–2–1–0.5–0.25 μg mL^{-1}.

Inoculation of bacterial suspension: daily cultures of reference strains in the McFarland 0.5 standard were used. They were diluted 100 times in nutrient broth, after which the concentration of microorganisms was approximately 106 CFU per mL. A working suspension (100 μL) was introduced into the wells. The final volume of the applied liquid in all wells was 200 μL. After adding all the components, the plates were closed with sterile lids and then incubated for 16–20 hours in a thermostat at 37 °C.

Registration of bacterial culture growth: at the end of incubation, bacterial growth was recorded using a FlexA-200 Microplate Reader flatbed photometer. The optical density was measured at a wavelength of 625 nm.

Calculation of the minimal inhibitory concentration (MIC): the average values of the optical density index of the suspension were calculated minus the value of the initial light transmission of the solution (before incubation) in each test cell: (1) negative growth control of a working suspension containing a reference antibiotic in a concentration equal to the minimum concentration of the studied substances; (2) control containing a bacterial suspension with a microorganism concentration of 5×10^5 CFU per mL; (3) each concentration of the studied substance. Based on the obtained optical density data, a graph of the activity dependence on the concentration of the drug was made. The minimum inhibitory concentration was the concentration of the drug at which the average light-transmission value of the suspension did not significantly exceed 1% of the average growth control value and/or the exit point of the curve became smooth.

Calculation of the minimum bactericidal concentration (MBC): to determine MBC, it was necessary to additionally determine the amount of CFU in the culture fluid in a well without visible growth. The MBC was taken to be the concentration of an antimicrobial compound, which reduced the number of viable cells by more than 3 orders (1000 times), or more than 99.9% of the pathogen cells died. From wells in which no bacterial growth was observed after MBC determination, 10 μL of the samples were inoculated onto plates with LB-agar and incubated for 24 hours. The MBC concentration was considered in those wells from which no bacterial growth occurred during inoculation. With an MBC/MIC ratio of 4 or less, the substance was considered to be bactericidal; with a MBC/MIC ratio of more than 4 times, the substance was bacteriostatic.

Assessment of hemolytic activity: HC_{50} μg mL^{-1} (the concentration causing 50% hemolysis) was determined using washed human erythrocytes. Samples were prepared in 96-well plates at varying concentrations (256–128–64–32–16–8–4 μg mL^{-1}) and incubated with the erythrocytes for 1 hour at 37 °C. Following incubation, the plates were centrifuged at 1000 rpm for 10 minutes, and the absorbance of the resulting supernatant was measured at 405 nm. The control (C) was a mixture of red blood cells with water (100% hemolysis). The intact control solution (S) was a mixture of erythrocytes with PBS and DMS. The antibiotic gramicidin was used as a control sample with active hemolysis. Absorption was measured using a FlexA-200 Microplate Reader flatbed photometer. Samples with hemolytic activity were characterized at $HC_{50} < 32$ μg mL^{-1}.

Assessment of antimicrobial activity against the biofilm-forming clinical isolates of the bacteria *Staphylococcus aureus* and *Enterococcus faecium* P-1 and the non-pathogenic strain

Pseudomonas fluorescens K-1: sterile beads for biofilm formation and a bacterial suspension at a concentration of 105 CFU per mL were inserted into the wells of a 96-well tablet. The tablets were incubated for 20 hours on a built-in incubator shaker at 37 °C. Balls with biofilms washed from a medium containing planktonic cells were transferred to a new tablet, with a medium containing serial double dilutions of compounds with concentrations of 256–128–64–32–16–8–4–2–1–0.5–0.25 μg mL^{-1}, and incubated for 18 hours at 37 °C. After incubation, the MIC that inhibited the growth of biofilms was determined.

The Minimum Biofilm Inhibitory Concentration (MBIC) was determined by culturing bacteria on carriers within the wells of a planchet, exposed to various substance concentrations (256–128–64–32–16–8–4–2–1–0.5–0.25–0.012–0.006 μg mL^{-1}) for 24 h at 37 °C. After incubation, the biofilms formed on the carrier surfaces were stained with a 0.1% aqueous crystal violet solution for 5 minutes, followed by extraction with ethanol for quantification. The intensity of biofilm formation was determined by the optical density of the obtained solutions at a wavelength of 595 nm and compared with that of the control.[43] Statistical data processing was carried out by Microsoft Excel.

Biofilms were grown using 96-well microtitre plate static assays. The wells of the microtitre plates were filled with 200 μL of fresh LB containing a 1 : 10 dilution of overnight cultures. 18 × 18 mm cover glasses were carefully broken into pieces of appropriate sizes and inserted perpendicularly into the wells to serve as substrates. The test compounds were added at the required concentrations (see the section on antimicrobial activity against the biofilm-forming clinical isolates of the bacteria). The plates were incubated without shaking at 37 °C for 16–24 h to allow biofilms to assemble at the air-liquid interface. The cover glass pieces with formed biofilms were removed from the wells using tweezers and washed by pipetting 50 μL of PBS over the substrate. Subsequently, the biofilms were stained with fluorescein (5 μg mL^{-1}). The prepared cover glass pieces were laid flat on fresh glass slides, covered with fresh 22 × 50 mm cover glasses, and fixed by taping the edges. Imaging was carried out using a Mikromed 3 LUM LED microscope. After focusing, wide-field views were captured, and biofilms were imaged at high magnification to resolve their structures at the cellular level.

Molecular docking methodology

Molecular docking simulations were performed to elucidate the precise mode of contact, key interacting residues, and binding affinity that underlined the antimicrobial efficacy of the synthesized ligands. The crystal structures of six essential bacterial target proteins, representing key metabolic and defense pathways, were retrieved from the RCSB Protein Data Bank (PDB): 5V8E (*B. cereus*), 2BL8 (*E. faecium*), 4PRV (*E. coli*), 1JIL (*S. aureus*), 1GWE (*M. luteus*), and 5V00 (*P. fluorescens*). Prior to docking, each protein structure was prepared by removing co-crystallized ligands and solvent molecules and adding both polar hydrogen atoms and Gasteiger partial charges using AutoDockTools.[44]

For ligand preparation, the chemical structures of the individual compounds were initially sketched using ChemDraw. Energy minimization was then executed using the MMFF94 s force field in Chem3D to obtain stable 3D conformations. The minimized ligand structures were subsequently converted into the *.pdbqt format by incorporating polar hydrogens and Gasteiger partial charges *via* AutoDockTools, making them compatible with the docking software.

The docking experiments, aimed at assessing the interaction and estimating the binding affinity of the target protein-compound complexes, were conducted using the AutoDock Vina v1.1.2 software.[45,46] To ensure the reliability of the protocol, docking validation was performed by re-docking the respective co-crystallized inhibitors back into the binding sites of the protein models. The successful re-docking was confirmed by calculating the Root Mean Square Deviation (RMSD) between the docked and native poses using DockRMSD,[47] where values below 2 Å were considered acceptable.

The docking parameters were consistently set for all simulations, utilizing a grid-box size of 24 × 24 × 24 $Å^3$ centered precisely around the known ligand-binding site. All other search parameters were maintained at the program's default settings. The pose exhibiting the lowest binding energy (kcal mol^{-1}) and establishing optimal interactions with the amino acid residues in the active site was selected as the best binding conformation. The final two-dimensional interaction maps, illustrating specific interactions, such as hydrogen bonds, Pi–Pi stacking, and Pi-cation contacts, were generated and visualized using the Discovery Studio Visualizer software.

Conclusions

Six novel heterocyclic azo compounds were isolated by the condensation of 9,10-phenanthrene quinone, squaric acid and ammonium 2,3,5,6-tetraoxo-4-nitropyridinate with 5-bromo-2-hydrazinopyridine, 2-hydrazine benzoic acid, 2-chloro-3-hydrazinopyrazine, and 2-hydrazino-4-phenylthiazole and characterized by a set of independent methods. The spectroscopic analysis (FT-IR and ^{1}H NMR) predicted the hydrazo-forms of all the studied molecules, which were proved by the DFT simulation method and the crystal structure determination of two species, *i.e.* 10-(3-(2-chloropyrazine-2-yl)hydrazinylidene) phenanthrene-9(10*H*)-one ($\mathbf{L^2}$) and 10-(2-(4-phenyl thiazo-2-yl) hydrazinylidene)phenanthrene-9(10*H*)-one ($\mathbf{L^4}$). The two molecules were found to be almost planar. Planarity was provided by strong, significant π-delocalization in the C2(C1)N1N2C12(C5) fragments of the molecules and by short N3H (2.51 Å) and Cl1H (2.49 Å) contacts in $\mathbf{L^4}$ and $\mathbf{L^2}$, respectively. The molecules were also stabilized by intramolecular N1H···O1 bonds. In the lattice, the molecules of $\mathbf{L^4}$ and $\mathbf{L^2}$ formed parallel layers arranged in columns, with no intermolecular H bonds. The stacks were arranged at van-der-Waals distances, which could not avoid the π,π-stacking between the planar parallel fragments in the columns.

Antimicrobial activity against biofilm-forming bacteria was determined using a turbidimetric method that controls the growth of microorganisms, and the values of the minimum

inhibitory concentration and minimum bactericidal concentration for Gram-positive and Gram-negative bacterial strains were calculated. The possibility of a hemolytic effect of the compounds on human red blood cells was evaluated. The performed studies allowed us to conclude that $\mathbf{L}^3$ and $\mathbf{L}^4$ exhibited strong bacteriostatic activity.

The ADMET analysis indicated that all the studied compounds obeyed Lipinski's and Veber's rules of the drug discovery pipeline: they possessed oral bioavailability and negative blood–brain barrier permeability, indicating their potential as therapeutic lead-like compounds.

Based on the results of Toxtree, all the compounds belonged to Class IV (low) toxic compounds.

Author contributions

Van Anh Nguyen: methodology; writing – original draft, writing – review & editing Thi Ngoc Anh Vu: data curation; writing – review & editing. Andrey Utenyshev. Minh Chin Huynh, Igor Filenko: investigation; formal analysis. Viktor Khrustalev: X-ray studies. Anton Shetnev: microbiological studies. Nadezhda Polyanskaya, Svetlana Bozhenkova: synthesis, investigation; validation. Olga Kovalchukova: supervision; writing – original draft, project administration, writing – review & editing.

Conflicts of interest

There are no conflicts to declare.

Data availability

Data for this article, including UV-vis, FTIR, and NMR spectral data, antimicrobial activity studies, DFT calculations, and single-crystal XRD and molecular docking simulation results, are available in the supplementary information (SI). Supplementary information is available. See DOI: https://doi.org/10.1039/d5ra10033j.

CCDC 2482127 and 2482128 contain the supplementary crystallographic data for this paper.[48a,b]

Acknowledgements

The studies were performed in accordance with the state assignment no. 124013100858-3 and supported by the RUDN Strategic Academic Leadership Program. All experiments were performed in accordance with the Guidelines of the Ethical Standards of Scientific Research, and experiments were approved by the ethics committee at the Yaroslavl State Pedagogical University named after K. D. Ushinsky (protocol no. 8 dated 14.01.2025). Informed consents were obtained from the human participants of this study.

References

1 M. Fesatidou, A. Petrou and G. Athina, *Curr. Pharm. Des.*, 2020, **26**(8), 867–904.
2 A. Cheddie, S. A. Shintre, A. Bantho, C. Mocktar and N. A. Koorbanally, *J. Heterocycl. Chem.*, 2020, **57**(1), 299–307.
3 M. Aatif, M. A. Raza, K. Javed, S. M. Nashre-ul-Islam, M. Farhan and M. W. Alam, *J. Antibiot.*, 2022, **11**(12), 1750.
4 J. K. Adu, C. D. K. Amengor, N. Mohammed Ibrahim, C. Amaning-Danquah, C. Owusu Ansah, D. D. Gbadago and J. Sarpong-Agyapong, *J. Trop. Med.*, 2020, **1**, 4850492.
5 I. B. Campbell, S. J. F. Macdonald and P. A. Procopiou, Medicinal chemistry in drug discovery in big pharma: past, present and future, *Drug Discovery Today*, 2018, **23**(2), 219–234.
6 K. Mezgebe and E. Mulugeta, Synthesis and pharmacological activities of azo dye derivatives incorporating heterocyclic scaffolds: a review, *RSC Adv.*, 2022, **12**(40), 25932–25946.
7 A. J. Jarad, I. Y. Majeed and A. O. Hussein, Synthesis and spectral studies of heterocyclic azo dye complexes with some transition metals, *J. Phys.:Conf. Ser.*, 2018, **1003**(1), 012021.
8 S. A. Hamid, Y. Ali and U. Rashid, Biomedical applications of aromatic azo compounds, *Mini-Rev. Med. Chem.*, 2018, **18**(18), 1548–1558.
9 S. Dinda, D. Maitra, B. Roy, P. Khan, A. Samajdar, A. K. Mitra and S. Ganguly, *ChemistrySelect*, 2022, **7**(34), e202202151.
10 G. Kanrar, S. Halder, S. Naskar, D. Jana, A. Sarkar, B. K. Panda and S. Ganguly, *J. Mol. Struct.*, 2024, **1314**, 138720.
11 S. B. Zaichenko, L. D. Popov, A. S. Burlov, V. G. Vlasenko, A. A. Kolodina, E. V. Korshunova and I. N. Shcherbakov, *Russ. J. Gen. Chem.*, 2022, **92**(6), 1011–1031.
12 S. Li, C. Gao, J. Xue, H. Xin, H. Li and J. Zhang, *Dyes Pigm.*, 2024, **224**, 112023.
13 J. Huang, Y. Chen, Y. Guo, M. Bao, K. Hong, Y. Zhang and X. Xu, *Mol. Diversity*, 2023, **27**(2), 845–855.
14 Y. Du, H. Zhao, X. Peng, X. Zhou, X. Yang, Y. Li and G. Sun, *J. Photochem. Photobiol., A*, 2023, **439**, 114604.
15 R. V. Linko, M. A. Ryabov, V. V. Davydov and V. N. Khrustalev, *Russ. J. Gen. Chem.*, 2023, **93**(8), 1998–2010.
16 G. G. Dias, E. R. Paz, M. P. Nunes, R. L. Carvalho, M. O. Rodrigues, F. S. Rodembusch and E. N. da Silva Júnior, *Chem. Rec.*, 2021, **21**(10), 2702–2738.
17 R. Kumar, P. P. Singh, Y. Murti, J. Gairola, S. Mahajan, H. Kandhari, P. K. Singh and V. Srivastava, *Synth. Commun.*, 2024, **54**(14), 1129–1146.
18 A. Karak, D. Banik, R. Ganguly, S. Banerjee, P. Ghosh, A. Maiti, D. Mandal and A. K. A. Mahapatra, *Chem. Res. Toxicol.*, 2024, **37**(5), 771–778.
19 V. M. Dembitsky and A. O. Terent'ev, *Microbiol. Res.*, 2025, **16**(5), 100.
20 V. V. Davydov, N. A. Polyanskaya, R. V. Linko, M. A. Ryabov, V. S. Sergienko and V. I. Sokol, *Crystallogr. Rep.*, 2012, **57**(2), 227–234.
21 R. V. Linko, N. A. Polyanskaya, M. A. Ryabov, V. V. Davydov, V. I. Sokol and V. S. Sergienko, *Russ. J. Inorg. Chem.*, 2013, **58**(2), 144–151.
22 R. V. Linko, N. A. Polyanskaya, M. A. Ryabov, V. V. Davydov, V. I. Sokol and V. S. Sergienko, *Russ. J. Inorg. Chem.*, 2013, **58**(3), 284–292.

23 R. V. Linko, N. A. Polyanskaya, M. A. Ryabov, P. V. Strashnov, V. V. Davydov, V. I. Sokol and V. S. Sergienko, *Crystallogr. Rep.*, 2013, **58**(3), 427–436.
24 R. V. Linko, N. A. Polyanskaya, M. A. Ryabov, V. V. Davydov, V. I. Sokol, V. S. Sergienko and P. V. Strashnov, *Russ. J. Inorg. Chem.*, 2013, **58**(12), 1457–1464.
25 R. V. Linko, N. A. Polyanskaya, M. A. Ryabov, V. V. Davydov, G. M. Drogova, V. S. Sergienko and P. V. Strashnov, *Russ. J. Coord. Chem.*, 2019, **45**, 1.
26 G. Roman, *Eur. J. Med. Chem.*, 2015, **89**, 743–816.
27 K. K. Palkina, N. E. Kuz'mina, O. V. Koval'chukova, S. B. Strashnova and B. E. Zaitsev, *Dokl. Chem.*, 2000, **370**(5), 631–634.
28 S. Kitagawa and S. Kawata, Coordination compounds of 1,4-dihydroxybenzoquinone and its homologues. Structures and properties, *Coord. Chem. Rev.*, 2002, **224**(1–2), 11–34.
29 O. Kovalchukova and S. Strashnova, Coordination chemistry of polyoxo-carbocyclic compounds containing one or more neighboring oxo-groups, *Rev. Inorg. Chem.*, 2014, **34**(1), 1–24.
30 J. Chasák, V. Šlachtová, M. Urban and L. Brulíková, *Eur. J. Med. Chem.*, 2021, **9**, 112872.
31 R. M. Silverstein and F. X. Webster, *Identification of Organic Compounds*, John Wiley & Sons, Inc., 6th edn, 1996.
32 A. Daina, O. Michielin and V. Zoete, SwissADME: a free web tool to evaluate pharmacokinetics, drug-likeness and medicinal chemistry friendliness of small molecules, *Sci. Rep.*, 2017, **3**(7), 42717.
33 F. Cheng, W. Li, Y. Zhou, J. Shen, Z. Wu, G. Liu, P. W. Lee and Y. Tang, AdmetSAR: a comprehensive source and free tool for assessment of chemical ADMET properties, *J. Chem. Inf. Model.*, 2012, **52**, 3099–10552.
34 H. Wan, What ADME tests should be conducted for preclinical studies?, *ADMET DMPK*, 2013, **1**(3), 19–28.
35 C. A. Lipinski, F. Lombardo, B. W. Dominy and P. J. Feeney, *Adv. Drug Delivery Rev.*, 2012, **64**, 4–17.
36 I. Karimi, N. Yakhchalian, M. Fathi and S. S. Miraghaee, *Univers. J. Pharm. Res.*, 2022, **7**, 74–80.
37 T. Lynch and A. P. Neff, *Am. Fam. Physician*, 2007, **76**, 391–396.
38 CrysAlisPro Software System, V. 1.171.41.106a, Rigaku Oxford Diffraction, 2021.
39 G. M. Sheldrick, *Acta Crystallogr.*, 2015, **A71**, 3–8.
40 G. M. Sheldrick, *Acta Crystallogr., Sect. C*, 2015, **71**(1), 3–8.
41 A. D. Becke, *J. Chem. Phys.*, 1993, **98**(7), 5648–5652.
42 A. Schaefer, C. Huber and R. Ahlrichs, *J. Chem. Phys.*, 1994, **100**(8), 5829–5835.
43 A. Granovsky, *Firefly Version 7.1.G*, https://classic.chem.msu.su/gran/firefly/index.html.
44 E. C. Adukwu, S. C. Allen and C. A. Phillips, The anti-biofilm activity of lemongrass (*Cymbopogon flexuosus*) and grapefruit (*Citrus paradisi*) essential oils against five strains of Staphylococcus aureus, *J. Appl. Microbiol.*, 2012, **113**(5), 1217–1227.
45 O. Trott and A. J. Olson, *J. Comput. Chem.*, 2010, **31**(2), 455–461.
46 J. Eberhardt, D. Santos-Martins, A. F. Tillack and S. Forli, *J. Chem. Inf. Model.*, 2021, **61**(8), 3891–3898.
47 E. W. Bell and Y. Zhang, *J. Cheminf.*, 2019, **11**(1), 40.
48 (*a*) CCDC 2482127: Experimental Crystal Structure Determination, 2026, DOI: 10.5517/ccdc.csd.cc2p9vmh; (*b*) CCDC 2482128: Experimental Crystal Structure Determination, 2026, DOI: 10.5517/ccdc.csd.cc2p9vnj.